

Radiative feedback from an early X-ray background

S.C.O. Glover,^{1,2} & P.W.J.L. Brand¹

¹ Institute for Astronomy, University of Edinburgh, Royal Observatory, Blackford Hill, Edinburgh, EH9 3HJ

² Department of Astrophysics, American Museum of Natural History, Central Park West at 79th Street, New York, NY 10024

21 May 2019

ABSTRACT

The first generation of stars (commonly known as population III) are expected to form in low-mass protogalaxies in which molecular hydrogen is the dominant coolant. Radiation from these stars will rapidly build up an extragalactic ultraviolet background capable of photodissociating H₂, and it is widely believed that this background will suppress further star formation in low-mass systems.

However, star formation will also produce an extragalactic X-ray background. This X-ray background, by increasing the fractional ionization of protogalactic gas, promotes H₂ formation and reduces the effectiveness of ultraviolet feedback.

In this paper, we examine which of these backgrounds has the dominant effect. Using a simple model for the growth of the UV and X-ray backgrounds, together with a detailed one-dimensional model of protogalactic chemical evolution, we examine the effects of the X-ray backgrounds produced by a number of likely source models. We show that in several cases, the resulting X-ray background is strong enough to offset UV photodissociation in large H₂-cooled protogalaxies. On the other hand, small protogalaxies (those with virial temperatures $T_{\text{vir}} < 2000\text{ K}$) remain dominated by the UV background in all of the models we examine.

We also briefly investigate the effects of the X-ray background upon the thermal and chemical evolution of the diffuse IGM.

Key words: cosmology:theory – galaxies: formation – molecular processes – radiative transfer

1 INTRODUCTION

In cosmological models based on cold dark matter (CDM), the first stars are believed to form within small protogalaxies, with virial temperatures $T_{\text{vir}} < 10^4\text{ K}$ (Couchman & Rees 1986; Haiman *et al.* 1996a; Tegmark *et al.* 1997). Cooling within these protogalaxies is dominated by molecular hydrogen, H₂, which forms via the gas-phase reactions



and



even in the absence of dust. Although the fractional abundance of H₂ that forms in this way is small, it is sufficient to allow for effective cooling and the formation of stars (Haiman *et al.* 1996a; Tegmark *et al.* 1997; Bromm *et al.* 1999; Abel *et al.* 2000).

As soon as massive stars form, however, they immediately begin to photoionize and photodissociate this H₂. Photoionization requires photons with energies greater than

15.4 eV, which are strongly absorbed by neutral hydrogen, and is only of importance within H II regions. Photodissociation, by contrast, occurs through the absorption of photons in the Lyman-Werner band system (Stecher & Williams 1967), with energies in the range 11.18 – 13.6 eV. These photons are not strongly absorbed by neutral hydrogen and can readily escape into the intergalactic medium (Omukai & Nishi 1999; Glover & Brand 2001).

Initially, many of these photons will be absorbed by intergalactic H₂, but its abundance is small and it is rapidly photodissociated (see section 4.4 below). Consequently, the onset of star formation is soon followed by the appearance of an ultraviolet background radiation field. This ultraviolet background acts to suppress further star formation by photodissociating H₂ within newly-forming protogalaxies. The effects of this background have been studied by a number of authors (Ciardi *et al.* 2000a,b; Haiman *et al.* 1996b, 1997, 2000; Machacek *et al.* 2001). In particular, Haiman *et al.* (2000) study the coupled problem of the evolution of the ultraviolet background and its feedback on the global star formation rate using a simple galaxy formation model based on the Press-Schechter formalism (Press & Schechter 1974). They find that cooling (and hence star formation) within

small protogalaxies is completely suppressed prior to cosmological reionization. Taken at face value, their results suggest that star formation within small, H₂-cooled protogalaxies is a transient phenomenon, with little impact on later stages of galaxy formation.

These conclusions, however, rest on the assumption that the only free electrons present in the protogalactic gas come from the small residual fraction remaining after cosmological recombination. This is important, as free electrons (and protons) catalyze H₂ formation, as we can see from equations 1 to 4. If the free electron abundance were significantly higher, then the H₂ formation rate would also be higher, offsetting the effects of photodissociation. At the very least, this would delay the suppression of star formation, and in principle could entirely negate it.

It is therefore important to determine whether there is any way in which an enhanced level of ionization could be produced. One possible source is the residual ionization that would remain after the recombination of H II regions produced by an earlier generation of stars. This has recently been studied by Ricotti *et al.* (2001a,b), who find that it can be an effective source of H₂ and can dramatically reduce the effectiveness of photodissociation feedback. However, their conclusions are still somewhat uncertain, both because their simulations are under-resolved (see figures 5–7 in Ricotti *et al.* 2001a) and because they neglect the effects of supernovae, which would act to disperse the gas and significantly lengthen the recombination timescale, thereby delaying the formation of H₂.

An alternative possibility is ionization by a high redshift X-ray background. At X-ray energies, the optical depth of the intergalactic medium (IGM) is small and any X-ray sources present will naturally generate an X-ray background. Moreover, X-rays can penetrate to large depths within newly-formed protogalaxies, allowing them to raise the fractional ionization throughout the gas.

The potential importance of such a background was first highlighted by Haiman *et al.* (2000), with high redshift quasars suggested as a possible source. Using a very simple model for a quasar-produced X-ray background, they showed that if quasars contribute more than 10% of the UV background, then the ionization produced by the associated X-ray background is sufficient to negate the effects of UV photodissociation. Indeed, they found evidence that such a background could actually promote cooling within the dense gas in the centres of protogalaxies. This scenario has not yet been firmly ruled out, but observational evidence suggests that quasars are unlikely to be present in sufficient number at high redshift (Pei 1995; Haiman *et al.* 1999).

Quasars, however, are not the only potential source of X-rays. Star formation also leads to the production of X-rays, primarily through the formation of massive X-ray binaries (Helfand & Moran 2001), but also through bremsstrahlung and inverse Compton emission from supernova remnants. These sources generate only a small fraction of the present-day X-ray background (Natarajan & Almaini 2000), but may become dominant at high redshifts.

In this paper, we examine the effects of the X-rays produced by these sources, both on the cooling of gas within virialized protogalaxies and also on the chemical and thermal evolution of the IGM. The outline of the paper is as follows. In section 2, we discuss the sources responsible for

producing the UV and X-ray backgrounds, and show how the build-up of these backgrounds can be computed. In section 3, we outline the method used to study the effect of this radiation on the primordial gas, and in section 4 apply it for a number of different X-ray source models. We present our conclusions in section 5.

2 THE UV AND X-RAY BACKGROUNDS

For an observer at redshift z_0 , we can write the mean specific intensity of the radiation background at an observed frequency ν_0 as (Madau *et al.* 1999)

$$J(\nu_0, z_0) = \frac{1}{4\pi} \int_{z_0}^{\infty} \varepsilon(\nu, z) e^{-\tau(\nu_0, z_0, z)} \frac{(1+z_0)^3}{(1+z)^3} \frac{dl}{dz} dz, \quad (5)$$

where $\nu = \nu_0(1+z)/(1+z_0)$, $\varepsilon(\nu, z)$ is the proper space-averaged volume emissivity, $\tau(\nu_0, z_0, z)$ is the optical depth at frequency ν_0 due to material along the line of sight from redshift z_0 to z and dl/dz is the cosmological line element. To solve this equation, we need to know how the emissivity and opacity evolve with redshift.

2.1 Emissivity

For simplicity, we write the space-averaged emissivity in terms of the global star formation rate as

$$\varepsilon_\nu = 1.08 \times 10^{-66} L(\nu, z) \dot{M}_* \text{ erg s}^{-1} \text{ cm}^{-3} \text{ Hz}^{-1}, \quad (6)$$

where $L(\nu, z)$ is the luminosity density per unit star formation rate (in solar masses per year), and \dot{M}_* is the global star formation rate, with units $M_\odot \text{ yr}^{-1} \text{ Mpc}^{-3}$.

In principle, $L(\nu, z)$ may be a complicated function of frequency and redshift. In practice, however, Lyman-Werner band emission is dominated by massive, short-lived OB stars and is closely correlated with the star formation rate (SFR), while X-ray emission is dominated by sources such as massive X-ray binaries and supernova remnants that are linked to the same massive stars, and is likewise closely correlated with the SFR. Consequently, we can neglect the redshift dependence of $L(\nu, z)$ to a first approximation. With this simplification, determining the emissivity breaks down into two independent problems: determining the global star formation rate as a function of redshift, and determining the luminosity density as a function of the star formation rate.

2.1.1 The star formation rate

Although we have observational constraints on the star formation rate up to $z \sim 5$, we have no direct constraints (and few indirect ones) at higher redshift. Consequently, any model of high redshift star formation must inevitably be highly theoretical. Moreover, this lack of constraints motivates us to choose as simple a model as possible; more complicated (and realistic) models can always be considered once our observational knowledge improves. A good example of this kind of simple model is the one used by Haiman *et al.* (2000); we adopt the same model here.

We assume that star formation proceeds primarily through starbursts, of duration t_{on} years, that are triggered

when galaxies first form. During the starburst, the star formation rate is assumed to be constant. The global star formation rate in this model is given by

$$\dot{M}_* = \frac{\epsilon f_b \Delta \rho_{\text{gal}}}{t_{\text{on}}} M_\odot \text{ yr}^{-1} \text{ Mpc}^{-3}, \quad (7)$$

where ϵ is the star formation efficiency, f_b is the baryon fraction (which we assume to be equal to Ω_b/Ω_m), and where $\Delta \rho_{\text{gal}}$ is the cosmological density of matter in newly-formed galaxies (with units of $M_\odot \text{ Mpc}^{-3}$). This latter quantity can be derived from

$$\frac{d\Delta \rho_{\text{gal}}}{dz} = \rho_m(z) \frac{dF}{dz}(z, T_{\text{crit}}) \quad (8)$$

where $\rho_m = 2.8 \times 10^{11} \Omega_m (1+z)^3 M_\odot \text{ Mpc}^{-3}$ is the cosmological matter density, and $F(z, T_{\text{crit}})$ is the total fraction of matter to be found in halos with virial temperatures greater than some critical temperature T_{crit} . This critical temperature represents the minimum temperature required for efficient cooling to be possible; to a first approximation, halos with $T_{\text{vir}} < T_{\text{crit}}$ are unable to cool, while those with $T_{\text{vir}} > T_{\text{crit}}$ cool rapidly and can form stars.

In general, T_{crit} will depend both on redshift (see, eg Tegmark *et al.* 1997) and on the intensities of the UV and X-ray backgrounds; understanding its evolution with redshift is the main goal of this paper. In section 3, we discuss how we go about determining T_{crit} ; for now, we assume that it is known. In this case, we can calculate $F(z, T_{\text{crit}})$ using the Press-Schechter formalism (Lacey & Cole 1993):

$$F(z, M_{\text{crit}}) = \text{erfc} \left[\frac{\delta_c(z)}{\sqrt{2}\sigma(M_{\text{crit}})} \right], \quad (9)$$

where $\delta_c(z)$ is the critical density threshold for collapse, $\sigma(M)$ is the square root of the variance of the cosmological density field, as smoothed on a mass scale M , and where M_{crit} is the mass of a protogalaxy with virial temperature T_{crit} . Although both δ_c and $\sigma(M)$ depend upon the choice of cosmological model, their behaviour is well-known, and the problem of determining $F(z, M_{\text{crit}})$ reduces to the relatively simple one of relating M_{crit} to T_{crit} .

To do this, we need to know the protogalactic density profile. Hydrodynamical simulations suggest that it is approximately isothermal (Abel *et al.* 2000), but representing it as a singular isothermal sphere is physically unrealistic due to the latter's infinite central density. Accordingly, we follow Haiman *et al.* and represent it as a truncated isothermal sphere (Shapiro *et al.* 1999). With this choice, we find that

$$M_{\text{crit}} = 1.5 \times 10^7 \left(\frac{T_{\text{crit}}}{1000 \text{ K}} \right)^{3/2} (1+z)^{-3/2} h^{-1} M_\odot. \quad (10)$$

To determine $\Delta \rho_{\text{gal}}(z)$, we must integrate equation 8 over a redshift interval $\Delta z(t_{\text{on}})$, corresponding to the duration of the starburst; hence,

$$\Delta \rho_{\text{gal}}(z) = \int_z^{z+\Delta z(t_{\text{on}})} \rho_m(z) \frac{dF}{dz}(z, T_{\text{crit}}) dz. \quad (11)$$

This simple model has a number of shortcomings. For instance, it assumes that the star formation efficiency ϵ and starburst duration t_{on} are both constant, independent of redshift or galaxy mass. It also assumes that each galaxy forms its stars in a single starburst and thus ignores the effects

of continuous star formation and of subsequent, merger-triggered starbursts.¹ Nevertheless, it has the virtue of simplicity, and is a good point from which to start our examination of the effects of the X-ray background.

2.1.2 The UV luminosity density

The ultraviolet flux of a star-forming galaxy is dominated by emission from young, massive O and B-type stars. These are short-lived, with the most massive having lifetimes of only a few Myr, and thus the ultraviolet luminosity density is closely correlated with the star formation rate. Its value depends upon the spectral properties of the newly-formed stellar population, and thus on their initial mass function (IMF), metallicity and age.

In a recent paper, Schaerer (2002) presents values for the photon flux in the Lyman-Werner bands calculated for a number of different metal-free stellar populations. If we assume that the spectrum within the bands is flat (a reasonable approximation), then we can convert this photon flux into a luminosity density. For a Salpeter IMF with minimum mass $M_{\text{min}} = 1 M_\odot$ and maximum mass $M_{\text{max}} = 100 M_\odot$ (model A in Schaerer 2002), we find that

$$L_\nu = 1.1 \times 10^{28} \text{ erg s}^{-1} \text{ Hz}^{-1} (M_\odot \text{ yr}^{-1})^{-1}. \quad (12)$$

Reducing M_{min} to the more conventional value of $0.1 M_\odot$ reduces this luminosity to

$$L_\nu = 4.3 \times 10^{27} \text{ erg s}^{-1} \text{ Hz}^{-1} (M_\odot \text{ yr}^{-1})^{-1}, \quad (13)$$

as we form a greater number of low mass stars that do not contribute significantly to the Lyman-Werner flux.

Both of these results assume that the dissociative flux has stabilized at its equilibrium value and is therefore proportional to the star formation rate. This equilibrium is typically established after only 2–3 Myr, so this is generally a good approximation, even for starbursts of relatively short duration.

The above figures are appropriate so long as we are dealing with stars formed out of *entirely* metal-free gas. Such stars are somewhat unusual, however, as the absence of carbon means that they are unable to generate energy via the CNO cycle, which otherwise would dominate energy production in stars of mass $M \gtrsim 1.1 M_\odot$. As a result, metal-free stars are hotter than their metal-enriched counterparts (Ezer & Cameron 1971; Cassisi & Castellani 1993; Tumlinson & Shull 2000; Cojazzi *et al.* 2000) and have harder spectra. A surprising consequence of this fact is that a low-metallicity stellar population will produce a larger dissociative flux than a metal-free population – the lower effective temperatures move the peak in the thermal emission from the most massive stars closer to the Lyman-Werner band, causing the ionizing flux to fall but the dissociative flux to rise.

We can use the data presented in Schaerer (2002) for a stellar population with $Z = 0.02 Z_\odot$ to examine the difference that this effect makes to the Lyman-Werner flux. Using the same IMF as in equation 12, we find that

$$L_\nu = 1.8 \times 10^{28} \text{ erg s}^{-1} \text{ Hz}^{-1} (M_\odot \text{ yr}^{-1})^{-1}. \quad (14)$$

¹ Although both of these can be mimicked to some extent by choosing a large value for t_{on} .

Thus, raising the metallicity increases the Lyman-Werner flux, but only by about 60–70%; as we will see in section 4.1, this has little effect on the evolution of T_{crit} .

Clearly, there are many possible models other than those considered here. Indeed, there is growing evidence that the IMF of population III stars is strongly biased towards high masses (Larson 1998; Abel *et al.* 2000; Bromm *et al.* 1999, 2002). However, this remains uncertain, and in this paper we have chosen to err on the side of caution and assume that the high-redshift IMF is similar to that at the present day.

2.1.3 The X-ray luminosity density

In a recent study, Helfand & Moran (2001) collate data on a number of local starburst galaxies and compare the 2–10 keV X-ray fluxes measured by *ASCA* with the 8–1000 μm infrared fluxes measured by *IRAS*. They find that a clear correlation exists, with the total X-ray and infrared fluxes related by

$$F_{\text{X}} \simeq 10^{-4} F_{\text{IR}}. \quad (15)$$

Similar correlations have previously been reported by David *et al.* (1992) and Rephaeli *et al.* (1995) for X-rays in the 0.5–4.5 keV and 2–30 keV energy bands respectively.

Theoretically, we would expect such a correlation, with both the X-ray and infrared emission tracing the underlying star formation rate. For the X-rays, this occurs because the emission is dominated by massive X-ray binaries (MXRBs): binary systems consisting of a massive OB star accreting onto a compact companion (a neutron star or black hole). X-ray emission from such systems generally switches on a few million years after the formation of the compact object, and the lifetime of the emitting phase is short, typically of the order of $(2 - 5) \times 10^4$ yr (Meurs & van den Heuvel 1989). These short timescales tie the emission closely to the underlying star formation rate (Ghosh & White 2001). The far-infrared flux, on the other hand, tracks star formation far more directly, being dominated by emission from dust heated by short-lived, massive stars.

To use this observed correlation to determine the X-ray luminosity of a star-forming galaxy as a function of its star formation rate, we use the result from the starburst models of Leitherer & Heckman (1995) that

$$L_{\text{IR}} \sim 1.5 \times 10^{10} \left(\frac{\text{SFR}}{1 \text{ M}_\odot \text{ yr}^{-1}} \right) L_\odot, \quad (16)$$

together with equation 15 to write the X-ray luminosity as (Helfand & Moran 2001)

$$L_{\text{X}} = 6 \times 10^{39} \left(\frac{\text{SFR}}{1 \text{ M}_\odot \text{ yr}^{-1}} \right) \text{ erg s}^{-1}. \quad (17)$$

We then assume that this result, based on local observations, remains valid as we move to higher redshifts.

Evidence that this is indeed the case is provided by the recent stacking analysis of individually undetected Lyman break galaxies in the *Chandra* Deep Field-North (Brandt *et al.* 2001). This analysis finds that the average rest frame luminosity of the Lyman break galaxies in the 2–8 keV energy band is $L_{\text{X}} = 3.2 \times 10^{41} \text{ erg s}^{-1}$. Assuming a typical star formation rate of $50 \text{ M}_\odot \text{ yr}^{-1}$ for these galaxies (Shapley *et al.* 2001), this corresponds to an X-ray luminosity of

$$L_{\text{X}} = 6.4 \times 10^{39} \left(\frac{\text{SFR}}{1 \text{ M}_\odot \text{ yr}^{-1}} \right) \text{ erg s}^{-1}, \quad (18)$$

consistent with the value derived above.² Although far from conclusive, this result suggests that we can extrapolate the locally observed correlation to at least as far as $z \simeq 4$.

Comparing our determination of L_{X} with a recent calculation by Oh (2001), we find a difference of a factor of ten in our results. Some of this disagreement is due to the difference in X-ray energy bands considered (0.2–10 keV in Oh (2001), compared to 2–10 keV here), but some must surely be due to intrinsic scatter in the observational data, suggesting that equation 17 should properly be regarded as an order of magnitude estimate of the true X-ray luminosity.

Given equation 17 for the X-ray luminosity as a function of the star formation rate, we calculate the X-ray luminosity density by assuming a template spectrum of power-law form

$$L_\nu = L_0 \left(\frac{\nu_0}{\nu} \right)^\alpha, \quad (19)$$

where $\hbar\nu_0 = 1 \text{ keV}$, and requiring that

$$L_{\text{X}} = \int_{\nu_1}^{\nu_2} L_\nu \, d\nu, \quad (20)$$

where $\hbar\nu_1 = 2 \text{ keV}$ and $\hbar\nu_2 = 10 \text{ keV}$.

Rephaeli *et al.* (1995) find that a weighted average of the galaxies in their sample gives a value for the spectral index of $\alpha = 1.5 \pm 0.3$. Adopting this value and solving for L_0 , we find that

$$L_0 = 3.4 \times 10^{22} \text{ erg s}^{-1} \text{ Hz}^{-1} \left(\text{M}_\odot \text{ yr}^{-1} \right)^{-1}. \quad (21)$$

Altering α changes L_0 , but never by more than 50% for values consistent with the Rephaeli *et al.* measurement. Clearly, individual galaxies may have spectra that differ markedly from this simple template, but it should be a reasonable approximation when averaging over a large number of galaxies.

2.1.4 Alternative X-ray models

The above model is simple, and empirically motivated, but does assume that the X-ray emission of high-redshift star-forming galaxies is very similar to that of starbursts observed locally. This is a reasonable assumption in the absence of evidence to the contrary, and is probably valid as long as massive X-ray binaries continue to dominate the galactic X-ray emission. However, it is quite possible that at high redshift some other type of source will come to dominate the emission, particularly if the number of binary systems is small, as is suggested by recent simulations (Abel *et al.* 2000). It is therefore prudent to consider the effects of other potential sources of X-rays.

The obvious candidates are supernova remnants (SNR); next to X-ray binaries, they are the most significant galactic sources (Helfand & Moran 2001). They can emit X-rays through a variety of different emission mechanisms, but at high redshift the most significant will be thermal

² Note that X-ray luminosity of equation 18 is measured in a slightly different energy band from that of equation 17, so the agreement between the two values is not quite as good as may at first appear. Nevertheless, the necessary correction is small, and the values agree to within 50%.

bremsstrahlung emission and non-thermal inverse Compton emission.

Thermal bremsstrahlung is produced by the hot gas within the SNR. Detailed modeling properly requires a hydrodynamical treatment (see, for example, Chevalier 1999), but for our purposes a simple parameterization suffices. We write the luminosity density as

$$L_\nu = f_x E_{51} N_{\text{sn}} F_{\text{br}}(\nu) \text{ erg s}^{-1} \text{ Hz}^{-1} (\text{M}_\odot \text{ yr}^{-1})^{-1}, \quad (22)$$

where

$$F_{\text{br}}(\nu) = 1.3 \times 10^{26} \left(\frac{h\nu_0}{kT_x} \right) \exp \left(\frac{-h\nu}{kT_x} \right), \quad (23)$$

and where $h\nu_0 = 1 \text{ keV}$, E_{51} is the explosion energy (in units of 10^{51} ergs), f_x is the fraction of this energy radiated as bremsstrahlung and T_x is the characteristic temperature of the emission. The number of supernovae per solar mass of stars formed is given by N_{sn} and depends on the IMF; for the standard Salpeter IMF adopted previously, $N_{\text{sn}} = 0.0075 \text{ M}_\odot^{-1}$.

For typical supernova parameters ($E_{51} = 1$ and an ambient density $n = 1 \text{ cm}^{-3}$), Helfand & Moran (2001) find that a fraction $f_x = 2 \times 10^{-4}$ of the explosion energy is radiated, at a characteristic temperature $T_x = 1 \text{ keV}$. On the other hand, the higher mean density at high redshift, together with the comparative weakness of outflows from low metallicity stars (Kudritzki 2000) suggest that the typical ambient density may be very much higher. In particular, if it is as high as $n \simeq 10^7 \text{ cm}^{-3}$, then a supernova remnant will radiate its energy extremely rapidly, before the ejecta have time to thermalize (Terlevich *et al.* 1992). In this case, the fraction of energy radiated as bremsstrahlung is very much higher ($f_x \simeq 0.01$), as is the characteristic temperature ($T_x \sim 30 \text{ keV}$). We examine both of these models in section 4, with the understanding that the true picture lies somewhere in between.

In addition to this thermal emission, supernova remnants also produce non-thermal X-rays. These are generated as the relativistic electrons produced by the SNR gradually lose energy through synchrotron radiation, non-thermal bremsstrahlung and the inverse Compton scattering of photons from the cosmic microwave background. At high redshift, the latter is likely to dominate (Oh 2001). The spectrum of the resulting emission depends upon the energy spectrum of the relativistic electrons, but at the energies of interest is well represented by a power law: $L_\nu \propto \nu^{-1}$. The intensity of the emission depends upon the fraction of the supernova energy transferred to the electrons; this is not well constrained, with estimates ranging from 0.1% to 10%. Accordingly, we model the emission as

$$L_\nu = 7.7 \times 10^{23} \left(\frac{\nu_0}{\nu} \right) f_e \text{ erg s}^{-1} \text{ Hz}^{-1} (\text{M}_\odot \text{ yr}^{-1})^{-1}, \quad (24)$$

where $h\nu_0 = 1 \text{ keV}$, f_e is the fraction of energy deposited in the electrons, and where we have assumed that $E_{51} = 1$ and $N_{\text{sn}} = 0.0075 \text{ M}_\odot^{-1}$ as in the thermal bremsstrahlung case. This expression assumes a high-energy cutoff for the X-ray spectrum at 10 keV but is only logarithmically dependent on the value of this cutoff. In section 4, we examine results for models with $f_e = 10^{-3}$ and $f_e = 0.1$, which bracket the range of plausible values.

Much more detail on high redshift inverse Compton

emission, including a discussion of potential observational tests, is given in Oh (2001).

2.2 Opacity

The opacity $\tau(\nu_0, z_0, z)$ can be separated into two distinct components – absorption by dust and gas within the emitting protogalaxy, which we term intrinsic absorption, and absorption by gas along the line of sight through the IGM.

Intrinsic absorption is difficult to model with any degree of accuracy as it depends upon a number of variables – the size and shape of the galaxy, its ionization state, the position of the sources within it, the dust content etc. Rather than attempt to model these in detail – a significant undertaking in itself – we instead adopt a highly approximate representation. We assume that the emitted X-rays are attenuated by absorption by a neutral hydrogen column density of $N_{\text{H}} = 10^{21} \text{ cm}^{-2}$ plus an associated neutral helium column density of $N_{\text{He}} = 0.08 N_{\text{H}}$. This absorption is assumed to be the same for all sources. These values are chosen because they are representative of the column densities of the protogalaxies studied in this paper (which presumably contain the bulk of the X-ray sources). However, our results are not particularly sensitive to the column density adopted.

We do not include intrinsic absorption of Lyman-Werner photons, as any H_2 within the star-forming protogalaxies will be rapidly destroyed (Glover & Brand 2001), allowing the photons to escape into the IGM.

In both cases, we assume dust absorption can be neglected; the dust content of initially primordial gas is clearly zero, while even in enriched gas dust absorption becomes significant only at high column densities.

Absorption due to gas in the IGM is far simpler to treat, particularly if we can assume that the bulk of the gas is still of approximately uniform density. This assumption is generally reasonable at high redshift for photons with mean free paths much greater than the typical clumping scale, as is the case for both Lyman-Werner band photons and X-rays. Our treatment is discussed in the following sections.

2.2.1 Lyman-Werner band absorption

The continuum opacity of metal-free gas is very small (Lenzuni *et al.* 1991) and for our purposes can be neglected. Consequently, the only significant sources of opacity encountered by Lyman-Werner photons are absorption by the Lyman series lines of neutral hydrogen, and by the Lyman-Werner lines of molecular hydrogen. The Lyman series lines have the effect of absorbing any Lyman-Werner photons of the same frequency, and reprocessing them to Lyman- α photons plus associated softer photons. As Lyman- α lies outside of the Lyman-Werner band, the net effect is to block from view any sources at redshifts higher than some maximum, z_{max} , given by

$$\frac{1 + z_{\text{max}}}{1 + z_0} = \frac{\nu_{\text{H}}}{\nu_0}, \quad (25)$$

where ν_{H} is the frequency of the appropriate Lyman series line and ν_0 and z_0 are the observed frequency and redshift. Clearly, the size of z_{max} depends upon the distance between ν_0 and ν_{H} , and thus more sources are seen at frequencies that are a long way from a line. As a result, the spectrum develops

a characteristic ‘sawtooth’ shape (see figure 1 in Haiman *et al.* 2000), with the effect becoming more pronounced as one nears the Lyman limit.

Absorption by molecular hydrogen is rather more complicated, due to the large number of Lyman-Werner lines that contribute to the opacity. If we approximate the lines as delta functions then an individual line produces an opacity

$$\tau_i = \frac{\pi e^2}{m_e c} f_{\text{osc},i} \lambda_i \frac{n_{\text{H}_2}(z_i)}{H(z_i)}, \quad (26)$$

where $f_{\text{osc},i}$ and λ_i are the oscillator strength and wavelength of the transition respectively, and $n_{\text{H}_2,i}$ is the number density of H_2 molecules in the level that gives rise to the line. The redshift at which the line is seen in absorption, z_i , is given by

$$\frac{1+z_i}{1+z_0} = \frac{\nu_i}{\nu_0}. \quad (27)$$

If we assume that all of the photons that are absorbed in the lines are permanently removed from the Lyman-Werner band, then the total opacity $\tau(\nu_0, z_0, z)$ is simply given by the sum over all lines with $z < z_i < z_{\text{max}}$:

$$\tau(\nu_0, z_0, z) = \sum_i \frac{\pi e^2}{m_e c} f_{\text{osc},i} \lambda_i \frac{n_{\text{H}_2}(z_i)}{H(z_i)}. \quad (28)$$

This sum potentially involves a very large number of lines, but can be greatly simplified by assuming that all of the H_2 is to be found in its ortho or para ground state; at the redshifts of interest, the population of excited states will be negligible.

In deriving this expression, we have assumed that every absorption permanently removes a Lyman-Werner band photon. This is not entirely correct. On average, only 15% of absorptions are followed by photodissociation of the H_2 molecule (Draine & Bertoldi 1996); the rest of the time, the molecule decays back to a bound state, emitting a photon. In their treatment of this problem, Haiman *et al.* (2000) assumed that the excited H_2 molecule would always decay directly back into the original state, and would thus emit a photon of the same energy as the one initially absorbed. In fact, this is not correct (T. Abel, private communication); most decays occur initially to highly excited vibrational states, producing photons redwards of the Lyman-Werner bands. Only a small fraction of decays (about 5%) take place directly into the original state, while a slightly larger fraction (about 15%) produce photons that lie elsewhere in the Lyman-Werner band system (Glover & Brand 2001). We do not include the effect of these photons, however; an accurate treatment would be quite complicated and is almost certainly unnecessary – as we shall see in section 4, H_2 in the IGM is rapidly destroyed by the growing Lyman-Werner background and is completely negligible by the time that negative feedback begins.

2.2.2 X-ray absorption

At X-ray energies, the opacity of the intergalactic gas is dominated by the ionization of neutral hydrogen and helium; prior to recombination, the He^+ abundance is small and can be neglected. The X-ray opacity can thus be written as

$$\tau(\nu_0, z_0, z) = \int_{z_0}^z [\sigma_{\text{H}}(\nu) n_{\text{H}} + \sigma_{\text{He}}(\nu) n_{\text{He}}] \frac{dl}{dz} dz, \quad (29)$$

where

$$\nu = \nu_0 \frac{(1+z)}{(1+z_0)}, \quad (30)$$

and where $\sigma_{\text{H}}(\nu)$ and $\sigma_{\text{He}}(\nu)$ are the absorption cross-sections of neutral hydrogen and helium respectively, with $n_{\text{H}}(z)$ and $n_{\text{He}}(z)$ being the corresponding number densities. As long as the fractional ionization of the IGM remains small, we can write this purely in terms of the neutral hydrogen number density as

$$\tau(\nu_0, z_0, z) = \int_{z_0}^z \left[\sigma_{\text{H}} + \left(\frac{Y}{4-4Y} \right) \sigma_{\text{He}} \right] n_{\text{H}} \frac{dl}{dz} dz, \quad (31)$$

where $Y = 0.247$ is the helium mass fraction. This integral is readily computable by means of numerical integration.

3 METHOD

In the previous section, we showed that, given a simple star formation model, it is relatively easy to calculate the evolution of the Lyman-Werner and X-ray backgrounds. Two of the parameters of our star formation model – the star formation efficiency ε and starburst lifetime t_{on} – we treat as free parameters (although they can be constrained to some extent – see, e.g. Haiman & Loeb 1997). The remaining parameter, T_{crit} , the temperature at which efficient cooling becomes possible, is determined by the strength of the backgrounds themselves. This clearly presents us with a problem: the evolution of T_{crit} is coupled to that of the backgrounds, and to know one we must first know the other.

Fortunately, this difficulty is easily avoided. We know that at high redshift the number of protogalaxies, and hence the star formation rate, must be very small. Consequently, there must be some redshift above which the background radiation will become too weak to affect galaxy formation. The precise redshift at which this occurs is model dependent, but for the models examined in this paper is typically about $z = 40$. By choosing an initial redshift $z_i = 50$, therefore, we can be sure that in our initial simulation the background radiation will have no effect.

Given this starting point, we next proceed incrementally to lower redshifts via the following procedure:

- (i) Given $T_{\text{crit}}(z_i)$, we calculate the background radiation field at $z = z_i - \Delta z$, assuming that $T_{\text{crit}}(z) = T_{\text{crit}}(z_i)$.
- (ii) Using the computed background, we simulate the chemical and thermal evolution of a protogalaxy with $T_{\text{vir}} = T_{\text{crit}}(z)$; the details of this simulation are outlined in sections 3.1 to 3.7 below. The main aim of this simulation is to determine whether the protogalactic gas can cool efficiently.
- (iii) If the protogalactic gas cools, then our assumed value of T_{crit} is correct; we store this result, and return to step one to proceed to the next redshift. If the gas fails to cool, we continue to step four.
- (iv) We increment our assumed value of $T_{\text{crit}}(z)$ by a small amount ΔT , and recalculate the background radiation field. We assume that T_{crit} varies linearly over Δz . Given the new background, we return to step two.

Provided that Δz and ΔT are both small, the error in $T_{\text{crit}}(z)$ will also be small; this is particularly the case once emission from larger protogalaxies (which cool via Lyman- α radiation) begins to dominate the background.

This approach reduces the coupled problem to the simpler one of determining whether a protogalaxy with virial temperature T_{vir} and formation redshift z_f will cool when exposed to a particular background radiation field. To answer this question, we need to be able to model the thermal and chemical evolution of the protogalaxy. Our approach to this problem is outlined in the following sections.

3.1 Computing the evolution of protogalactic gas

Ideally, we would like to use a high-resolution hydrodynamical simulation to follow the thermal and chemical evolution of the protogalactic gas (see, e.g. Machacek *et al.* 2001). Unfortunately, including the effects of radiative transfer, particularly of photons in the Lyman-Werner bands, into such a simulation is not currently feasible. We are thus forced to approximate. In choosing an appropriate approximation, we are also motivated by the desire to minimize the computational requirements of our simulations, so that we can explore the effects of a variety of different source models. We make three main approximations:

(i) We assume spherical symmetry. This is a reasonable approximation for the first generation of protogalaxies, but clearly is incorrect in detail (see, e.g. figure 2 of Abel *et al.* 2000).

(ii) We assume that the protogalactic gas is *static*, at least on the timescale of the simulation. This allows us to ignore the hydrodynamical evolution of the gas, and also substantially simplifies the treatment of radiative transfer. This assumption clearly breaks down once the gas begins to cool strongly and loses its pressure support, but as we are only interested in the evolution up to this point, this is not a significant problem.

(iii) We assume that all of the H₂ molecules remain in the rotational and vibrational ground state, in either ortho or para form. This simplification allows us to evolve the chemistry and radiative transfer on the timescale on which the total H₂ abundance changes (typically 10¹¹ – 10¹² s) rather than that on which the individual level populations change (10⁶ – 10¹⁰ s). It also simplifies our treatment of the radiative transfer. We discuss this approximation in more detail in section 3.4.2.

Together, these approximations allow us to solve for the chemical and thermal evolution of a model protogalaxy in a matter of minutes on a fast desktop computer. This allows us to study the redshift evolution of T_{crit} at high resolution in both temperature and redshift and for a number of different X-ray source models.

However, this approach has an obvious drawback – we cannot be sure that our approximations give a fair representation of the real protogalaxy. Of particular concern is the neglect of the hydrodynamic evolution of the gas, and the consequent error in the density profile. This is potentially significant because the H₂ cooling rate, along with many of the chemical reaction rates, scales as the square of the density. Small errors in the density can thus lead

to larger ones in the computed temperature. These concerns are mitigated to some extent, however, by the close agreement between the results of detailed numerical simulations and previous semi-analytic treatments. For instance, the values of T_{crit} obtained from the smoothed-particle hydrodynamics simulations of Fuller & Couchman (2000) agree well with the results of Tegmark *et al.* (1997), despite the highly approximate uniform density profile adopted by the latter group. Similarly, the results of Machacek *et al.* (2001), obtained with a three-dimensional adaptive mesh hydrodynamical code broadly agree with those of Haiman *et al.* (2000), who use a static model similar to that presented here. Together, these results suggest that T_{crit} is insensitive to the precise details of the density profile, but clearly this remains an area of concern.

Our computational method can be broken down into three main stages – initialization of the density profile and the chemical abundances, computation of the thermal and chemical evolution of the gas, and termination of the simulation at a suitable point. These are described below.

3.2 The model protogalaxy

The protogalactic density profile is modeled as a truncated isothermal sphere, with central overdensity $\delta = 1.796 \times 10^4$ and truncation radius

$$r_t = 4.62 \times 10^3 \left(\frac{T_{\text{vir}}}{1000 \text{ K}} \right)^{1/2} (1 + z_f)^{-3/2} h^{-1} \text{ pc.} \quad (32)$$

The virial temperature and redshift of formation of the protogalaxy completely specify its density profile.

We subdivide this profile into N_g spherical shells of uniform thickness and compute the mean density within each shell. We have run a number of test simulations with different values of N_g , and find that setting $N_g = 100$ provides sufficient spatial resolution to accurately determine T_{crit} .

We assume that the initial chemical composition of the protogalactic gas is the same as that of the intergalactic medium. At our initial redshift ($z = 50$), we take this from Stancil *et al.* (1998). At lower redshifts, the chemical evolution of the IGM is influenced by the Lyman-Werner and X-ray backgrounds. We therefore calculate the intergalactic abundances explicitly, using the chemical model outlined in section 3.3, by solving the chemical rate equations:

$$\frac{dn_i}{dt} = C_i(n_j, T) - D_i(n_j, T)n_i, \quad (33)$$

where C_i and D_i are source and sink terms for n_i . At the same time we also solve for the temperature of the intergalactic gas (Galli & Palla 1998)

$$\frac{dT}{dt} = -2TH(z) + \frac{2}{3kn_{\text{tot}}} (\Gamma - \Lambda), \quad (34)$$

where $H(z)$ is the Hubble constant, n_{tot} is the total particle number density and where Γ and Λ are the net heating and cooling rates (see section 3.5).

We solve this set of ordinary differential equations with the STIFBS integrator of Press *et al.* (1986). As the size of the required timestep is generally much smaller than the redshift interval Δz that separates our individual determinations of T_{crit} , we compute intermediate values by interpolation and from these determine the strength of the radiation background and hence the photochemical rates. Although our

main aim in following this chemistry is to determine the correct initial abundances for our simulations of protogalactic evolution, the results are of interest in their own right and are presented and discussed in section 4.4.

Our treatment of the chemistry of the IGM does not include the effects of the ionizing photons from stars (and/or quasars) that are ultimately responsible for the reionization of the intergalactic gas. This is justified at early epochs, as these photons are confined within small H II regions surrounding the luminous sources, but this simplification restricts the validity of our results to the period prior to cosmological reionization. The post-reionization epoch, and the effect of reionization on galaxy formation, have received extensive study elsewhere (see Loeb & Barkana 2001, and references therein).

3.3 The chemical model

To simulate the chemical evolution of the protogalactic gas, we adopt a chemical model consisting of thirty reactions between nine species: H, H⁻, H⁺, He, He⁺, He⁺⁺, H₂, H₂⁺ and free electrons. The reactions included in the model are summarized in table 1, together with the source(s) of the data used. This model is based in large part on that of Abel *et al.* (1997), but has been modified to improve its accuracy when applied to optically thick gas. Aside from a number of updates to the reaction coefficients in the light of new data, the main differences are as follows:

(i) We include the contribution to the hydrogen ionization rate arising from the ionizing photons produced by He⁺ recombination, in line with the discussion in chapter 2 of Osterbrock (1989). Although commonly a small correction to the total rate, this can become significant when X-ray photoionization dominates.

(ii) To enable us to accurately determine the He⁺ abundance, we find that we need to include the effects of charge transfer between He⁺ and H (reaction 20), as this can be comparable to the recombination rate when the fractional ionization is small. For completeness we also include the inverse reaction (no. 21), although this is unimportant at $T < 10^4$ K.

(iii) We include the contribution to the ionization rates of hydrogen and helium arising from secondary ionization by energetic photoelectrons, based on the recent calculations of Dalgarno *et al.* (1999). The contribution of secondary ionization to the other photoionization rates is small and can be neglected.

(iv) We do not include the photodissociation of H₂ by photons above the Lyman limit (reaction 28 in Abel *et al.*), as in optically thick gas this will be negligible compared to the effects of H₂ photoionization (reaction 26). On the other hand, we do include the effects of dissociative photoionization (reaction 27), which becomes significant for photon energies greater than 30 eV.

More information about all of these points, and the chemical model generally, can be found in Glover (2001).

3.4 Radiative transfer

In order to determine rate coefficients for the photochemical reactions (nos. 22–30), we need to calculate the evolution of

No.	Reaction	Reference
1.	H + e \rightarrow H ⁺ + 2e	Janev <i>et al.</i> (1987)
2.	H ⁺ + e \rightarrow H + γ	Ferland <i>et al.</i> (1992)
3.	He + e \rightarrow He ⁺ + 2e	Janev <i>et al.</i> (1987)
4.	He ⁺ + e \rightarrow He ⁺⁺ + 2e	Abel <i>et al.</i> (1997)
5.	He ⁺ + e \rightarrow He + γ	Hummer & Storey (1998), Aldrovandi & Pequignot (1973)
6.	He ⁺⁺ + e \rightarrow He ⁺ + γ	Ferland <i>et al.</i> (1992)
7.	H + e \rightarrow H ⁻ + γ	Wishart (1979)
8.	H ⁻ + H \rightarrow H ₂ + e	Launay <i>et al.</i> (1991)
9.	H + H ⁺ \rightarrow H ₂ ⁺ + γ	Ramaker & Peek (1976)
10.	H ₂ ⁺ + H \rightarrow H ₂ + H ⁺	Karpas <i>et al.</i> (1979)
11.	H ₂ + H ⁺ \rightarrow H ₂ ⁺ + H	Holliday <i>et al.</i> (1971)
12.	H ₂ + e \rightarrow 2H + e	Stibbe & Tennyson (1999)
13.	H ₂ + H \rightarrow 3H	Martin <i>et al.</i> (1996)
14.	H ⁻ + e \rightarrow H + 2e	Janev <i>et al.</i> (1987)
15.	H ⁻ + H \rightarrow 2H + e	Janev <i>et al.</i> (1987)
16.	H ⁻ + H ⁺ \rightarrow 2H	Moseley <i>et al.</i> (1970)
17.	H ⁻ + H ⁺ \rightarrow H ₂ ⁺ + e	Poulaert <i>et al.</i> (1978)
18.	H ₂ ⁺ + e \rightarrow 2H	Schneider <i>et al.</i> (1994)
19.	H ⁻ + He \rightarrow H + He + e	Huq <i>et al.</i> (1982)
20.	He ⁺ + H \rightarrow He + H ⁺ + γ	Zygelman <i>et al.</i> (1989)
21.	He + H ⁺ \rightarrow He ⁺ + H	Kimura <i>et al.</i> (1993)
22.	H + γ \rightarrow H ⁺ + e	Osterbrock (1989)
23.	He + γ \rightarrow He ⁺ + e	Yan <i>et al.</i> (1998)
24.	He ⁺ + γ \rightarrow He ⁺⁺ + e	Osterbrock (1989)
25.	H ⁻ + γ \rightarrow H + e	de Jong (1972)
26.	H ₂ + γ \rightarrow H ₂ ⁺ + e	O'Neil & Reinhardt (1978), Wilms <i>et al.</i> (2000), Yan <i>et al.</i> (1998)
27.	H ₂ + γ \rightarrow H + H ⁺ + e	Samson & Haddad (1994)
28.	H ₂ ⁺ + γ \rightarrow H + H ⁺	Dunn (1968)
29.	H ₂ ⁺ + γ \rightarrow 2H ⁺ + e	Bates & Öpik (1968)
30.	H ₂ + γ \rightarrow H ₂ [*] \rightarrow 2H	See text

Table 1. A list of the reactions included in our chemical model of protogalactic gas. Values for the rate coefficients (or radiative cross-sections where appropriate) are given in Glover (2001). References are to the primary source(s) of the data whenever possible; in many cases, we have also used analytical fits to this data from Abel *et al.* (1997), Galli & Palla (1998) or Stancil *et al.* (1998).

the mean specific intensity J_ν within the protogalactic gas. For optically thin gas, this is simple, but the only photochemical reactions for which we can assume optically thin conditions are H⁻ photodetachment (reaction 25) and H₂⁺ photodissociation (reaction 28); for the rest, we must supplement our chemical model with a treatment of radiative transfer.

The high degree of symmetry of the problem makes direct solution of the radiative transfer equation feasible, but the large spectral resolution required to properly treat the Lyman-Werner lines ($\Delta\nu/\nu \simeq 10^{-5}$) makes such an approach very time-consuming, particularly since it must be repeated for a very large number of timesteps. This motivates our choice of a much simpler approximate treatment that nevertheless should produce results of an acceptable accuracy.

We begin by assuming that the re-emission and/or scattering of photons within the protogalactic gas is negligible; in the absence of dust, this is a reasonable approximation.

This allows us to write the radiative transfer equation for an arbitrary line of sight through the protogalaxy

$$\frac{dI_\nu}{ds} = -\kappa_\nu(s)I_\nu + j_\nu(s), \quad (35)$$

(where κ_ν and j_ν are the opacity and emissivity respectively, and where s is the position along the line of sight) in the simpler form

$$\frac{dI_\nu}{ds} = -\kappa_\nu(s)I_\nu, \quad (36)$$

which can be further simplified to

$$\frac{dI_\nu}{d\tau_\nu} = -I_\nu. \quad (37)$$

Solution of this equation is trivial; if the specific intensity at the edge of the protogalaxy is $I_\nu(0)$, then at a distance s into the protogalaxy, it is

$$I_\nu = I_\nu(0)e^{-\tau_\nu(s)}. \quad (38)$$

To obtain the mean specific intensity, we simply integrate this expression over solid angle. Using the conventional variables r and μ (see figure 1), we find that

$$J_\nu(r) = \frac{1}{2}J_\nu(r_t) \int_{-1}^{+1} \exp[-\tau(\nu, r, \mu)] d\mu, \quad (39)$$

where $J_\nu(r_t)$ is the incident intensity at the edge of the protogalaxy (i.e. the background radiation) and where $\tau(\nu, r, \mu)$ is the optical depth between r and the edge of the protogalaxy in the direction of μ .

3.4.1 Photoionization

For the photoionization reactions (numbers 22–24, 26–27 & 29), the opacity is dominated by continuum absorption by neutral hydrogen and helium. For static gas, we can write this as

$$\tau(\nu, r, \mu) = \sigma_H(\nu)N_H(r, \mu) + \sigma_{He}N_{He}(r, \mu) \quad (40)$$

$$= \left[\sigma_H + \left(\frac{Y}{4-4Y} \right) \sigma_{He} \right] N_H(r, \mu), \quad (41)$$

where the second line follows if we assume primordial abundances and a small fractional ionization (which also allows us to neglect He^+ absorption).

Substituting this expression into equation 39, we obtain

$$J_\nu(r) = \frac{1}{2}J_\nu(r_t) \exp \left[- \left(\sigma_H + \frac{Y}{4-4Y} \sigma_{He} \right) \right] \mathcal{N}(r), \quad (42)$$

where

$$\mathcal{N}_H(r) = \int_{-1}^{+1} \exp[-N_H(r, \mu)] d\mu. \quad (43)$$

Aside from $\mathcal{N}_H(r)$, all of the terms in equation 42 are known at the beginning of the simulation. Moreover, if we assume that $J_\nu(r_t)$ remains constant for the duration of the simulation, then it becomes possible to calculate the photoionization rates in advance, tabulating them as functions of \mathcal{N}_H . If we do this, then instead of solving directly for the set of photoionization rates at each timestep, we can simply calculate $\mathcal{N}_H(r)$ and then interpolate the rates from the appropriate tables; this avoids a large number of frequency integrations, and results in a significant speed-up.

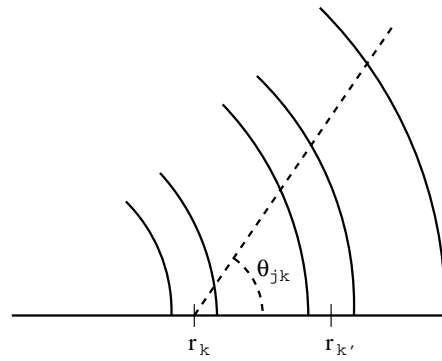


Figure 1. A schematic diagram of the radiative transfer geometry used in our simulations. For each of the N_g mass shells, we pick a single central point (r_k and $r_{k'}$ above are two examples) and compute column densities along N_a lines of sight to this point. With each line of sight, we can associate an angle θ (again, see the example above); however, it is generally simpler to work in terms the direction cosine $\mu = \cos \theta$.

3.4.2 Photodissociation

For Lyman-Werner photons, the situation is a little more complicated, due to the large number of spectral lines involved. Fortunately, there is a simple approach that we can use which significantly reduces the amount of computation required to obtain the photodissociation rate.

We begin by writing the total H_2 photodissociation rate as a sum of the contributions from each individual rotational and vibrational level:

$$k_{\text{dis}} n_{\text{H}_2} \equiv \sum_j k_j n_j, \quad (44)$$

where n_{H_2} is the total number density of H_2 molecules, and n_j is the number density of molecules in the j -th ro-vibrational level. For each level, we can write the photodissociation rate in the form (Draine & Bertoldi 1996)

$$k_j = \frac{2\pi J_\nu(r_t)}{h} \int_{-1}^{+1} \sum_i \frac{dW_{ij}}{dN_{\text{H}_2,j}} d\mu, \quad (45)$$

where W_{ij} is the dimensionless equivalent width of the i -th Lyman-Werner line originating from level j and where $N_{\text{H}_2,j}$ is the column density of H_2 molecules in level j . The equivalent width can be written as

$$W_{ij} = \int_0^\infty [1 - \exp(-\sigma_i(\nu)N_{\text{H}_2,j})] \frac{d\nu}{\nu}, \quad (46)$$

where the radiative cross-section $\sigma_i(\nu)$ can be written in terms of the line profile $\phi(\nu, \nu_i)$ and oscillator strength $f_{\text{osc},i}$ as

$$\sigma_i(\nu) = \frac{\pi e^2}{m_e c^2} f_{\text{osc},i} \phi(\nu, \nu_i). \quad (47)$$

In general, the form of the line profile will depend upon the details of the temperature and velocity variations along the line of sight. For static, isothermal gas, however, it reduces to the familiar Voigt profile. Consequently, $\sigma_i(\nu)$ is known *a priori*, allowing us to tabulate W_{ij} , and hence $dW_{ij}/dN_{\text{H}_2,j}$, as functions of $N_{\text{H}_2,j}$ at the beginning of the simulation. Similarly, we can tabulate the photodissociation rates k_j as a function of

$$\mathcal{N}_{\text{H}_2,j}(r) = \int_{-1}^{+1} \sum_i \frac{dW_{ij}}{dN_{\text{H}_2,j}} d\mu. \quad (48)$$

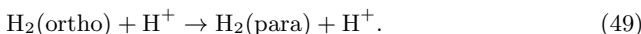
In this way, we reduce the problem of determining the photodissociation rates to the simpler one of determining the column density of H_2 molecules in each ro-vibrational level for a large number of lines of sight. Given a set of column densities for a particular level, we can obtain the corresponding values of $dW_{ij}/dN_{\text{H}_2,j}$ by interpolation; from these, we can derive $\mathcal{N}_{\text{H}_2,j}(r)$ by numerical integration; and finally, the photodissociation rate k_j is obtained by another interpolation.

Two potential problems remain with this method, however. Firstly, equation 46 breaks down at high column densities as two effects that we have neglected – absorption by neutral hydrogen, and overlap of the individual Lyman-Werner lines – become significant. Fortunately, these effects occur at column densities much higher than those we encounter in our simulations, so it is generally safe to ignore them.³

The second and more significant problem is the fact that, in the method as outlined, we have to deal with all of the rotational and vibrational levels of H_2 . This makes calculating the photodissociation rate much more costly than calculating the photoionization rates, as we need to compute several hundred different column densities for each line of sight. Similarly, the chemical network is also greatly enlarged and consequently takes longer to solve. Moreover, the excited vibrational levels typically have characteristic timescales of the order of 10^6 s, much smaller than the timescale on which the total H_2 abundance changes, forcing us to solve the chemical network with a timestep that is orders of magnitude smaller than we could otherwise use.

To overcome these problems, we make another approximation. Since, at the temperatures and densities encountered in our simulations, most of the excited levels have very small populations, their net contribution to the photodissociation rate is also very small. We can therefore safely ignore them, and concentrate only on the few rotational levels that are responsible for the bulk of the photodissociation.

The simplest approximation that we can make is to assume that all of the H_2 molecules are in the form of para-hydrogen and are to be found in the ground state. This approximation was suggested by Abel *et al.* (1997), and supposes that any ortho-hydrogen formed will be rapidly converted to para-hydrogen by collisions with protons (Gerlich 1990)



Unfortunately, this is only valid at very low temperatures, typically $T \lesssim 50$ K. At higher temperatures, conversion from para-hydrogen back to ortho-hydrogen via the inverse reaction becomes competitive. Moreover, at realistic temperatures and densities, ortho-para interconversion via proton collisions with excited states will also occur, and in general the ortho to para ratio will be close to its equilibrium value of three to one.

We can therefore obtain a much better approxima-

³ In any case, it is possible to reformulate equation 46 so as to avoid these problems, as in Draine & Bertoldi (1996).

tion to the true photodissociation rate by including ortho-hydrogen. For simplicity, we assume that the ortho to para ratio is fixed and is exactly three to one. We continue to ignore the other excited rotational levels.

Comparing the results of simulations performed using this approximation with those of simulations in which the rotational and vibrational level populations are set to their local thermodynamic equilibrium (LTE) values, we find that it performs fairly well. Although differences in the final H_2 abundance are observed, the effect on the evolution of T_{crit} is very small. Since the true level populations will lie somewhere between our simple approximation and the LTE case, this suggests that our approximation is sufficient for our purposes, and that a more detailed (and hence slower) treatment is not required.

3.4.3 Calculating the column densities

As demonstrated in the previous sections, we can determine the photochemical reaction rates for a given mass shell by computing the functions

$$\mathcal{N}_{\text{H}}(r) = \int_{-1}^{+1} \exp[-N_{\text{H}}(r, \mu)] d\mu, \quad (50)$$

and

$$\mathcal{N}_{\text{H}_2,j}(r) = \int_{-1}^{+1} \sum_i \frac{dW_{ij}}{dN_{\text{H}_2,j}} d\mu, \quad (51)$$

(where $j = 0, 1$ for the para and ortho-hydrogen ground states respectively) and then interpolating the rates from a pre-built look-up table. Moreover, knowledge of $N_{\text{H}}(r, \mu)$ and $N_{\text{H}_2,j}(r, \mu)$ is sufficient to specify $\mathcal{N}_{\text{H}}(r)$ and $\mathcal{N}_{\text{H}_2,j}(r)$ respectively, so the problem is essentially reduced to one of calculating these column densities.

To do this, we use a method very similar to that in Kepner *et al.* (1997). For each mass shell k , we choose a point r_k at the centre of the shell (see figure 1). For each of these points, we compute the column densities along N_a lines of sight with uniform angular separation. The column density of a chemical species i along one of these lines of sight is given by

$$N_i(r, \mu) = \int_0^L n_i[r'(x)] dx, \quad (52)$$

where $L = r\mu + [r_t^2 - r^2(1 - \mu^2)]^{1/2}$ is the total distance along the ray to the edge of the protogalaxy, and where $r'(x) = (r^2 + x^2 - 2rx\mu)^{1/2}$ is the distance from the point labeled by x to the centre of the protogalaxy. Solution of this equation by means of numerical integration is straightforward.

Given the set of column densities for a particular point r_k , we use equations 50 and 51 to compute $\mathcal{N}_{\text{H}}(r_k)$ and $\mathcal{N}_{\text{H}_2,j}(r_k)$, and then finally use these values to compute the photochemical rates at that point. Finally, the spherical symmetry of the problem allows us to generalize these rates to the whole of the mass shell containing r_k .

The accuracy of this procedure clearly depends both upon the spatial resolution of the grid (N_g) and upon the angular resolution with which we sample it (N_a). However, as the density, temperature and chemical abundances all vary smoothly within the protogalaxy, we find that very high resolution is not required: setting $N_g = 100$ and $N_a = 20$ proves

to be sufficient for accurate calculation of the photochemical rates. Simulations run with substantially higher values produce very similar results.

3.5 Heating and cooling

The heating and cooling processes included in our model are listed in table 2, together with references to the sources for the rates adopted. At low temperatures, cooling is dominated by rotational and vibrational line emission from H_2 ; we include this according to the recent prescription of Le Bourlot *et al.* (1999), which is probably the most accurate available to date. We do not include the effects of HD cooling: this becomes significant only at very low temperatures, and in any case does not appear to have a great effect on the evolution of the gas (Bromm *et al.* 2002).

At high temperatures ($T \gtrsim 8000$ K), cooling through the atomic lines of hydrogen (often referred to simply as Lyman- α cooling) rapidly becomes dominant. This sets an upper limit on T_{crit} ; for simplicity, we neglect any redshift dependence of this limit, and assume that protogalaxies with $T_{\text{vir}} \gtrsim 8000$ K can always cool successfully.

Heating of the protogalactic gas is driven primarily by the photoionization of hydrogen and helium. H_2 photodissociation also contributes to the heating rate, but is generally not significant, due to the small H_2 abundance.

3.6 Running the simulation

Given the initial temperature and chemical abundances, plus the set of chemical reaction rates, actually solving for the thermal and chemical evolution is relatively easy. As in the IGM case, we simply solve the coupled set of chemical rate equations

$$\frac{dn_i}{dt} = C_i(n_j, T) - D_i(n_j, T)n_i, \quad (53)$$

$$\frac{dT}{dt} = \frac{2}{3kn_{\text{tot}}} (\Gamma - \Lambda), \quad (54)$$

using the STIFBS integrator of Press *et al.* (1986).

At the start of each timestep (hereafter time t), we compute the photochemical rates as outlined in sections 3.4. We then use STIFBS to solve for the new chemical abundances and new temperature at the end of the timestep (time $t + \Delta t$), repeating this for each shell in turn. We next store these values, return to time t , and recalculate them using the same procedure, but with *two* timesteps of length $\Delta t/2$. We recalculate the photochemical rates at the intermediate point.

We next test for convergence by comparing our two sets of results. If any of the chemical abundances or temperatures of any of the shells differ by more than 0.1%, then we reject the results and begin again from time t with a smaller timestep. Otherwise, we check to see whether we need to halt the simulation, using the criteria discussed below, and, if we do not, we begin the computations for a new timestep starting from $t + \Delta t$.

One final approximation that we find useful in practice is to fix the H^- and H_2^+ abundances at their equilibrium values. This allows the integrator to take much larger timesteps than would otherwise be possible, but introduces very little error into the computed H_2 abundances.

Process	Reference
Atomic line cooling:	
H_I	Cen (1992)
He_I	Bray <i>et al.</i> (2000)
He_{II}	Aggarwal <i>et al.</i> (1992)
Molecular line cooling:	
H_2	Le Bourlot <i>et al.</i> (1999)
Collisional ionization:	
H_I	Janev <i>et al.</i> (1987)
He_I	Janev <i>et al.</i> (1987)
He_{II}	Abel <i>et al.</i> (1997)
Recombination:	
H_{II}	Ferland <i>et al.</i> (1992)
He_{II}	Aldrovandi & Pequignot (1973)
He_{III}	Ferland <i>et al.</i> (1992)
Other chemistry:	
H^- formation	Shapiro & Kang (1987)
H_2^+ formation	Shapiro & Kang (1987)
Bremsstrahlung:	
	Spitzer (1978)
Compton scattering:	
	Peebles (1993)
Photoionization:	
H_I	Osterbrock (1989), Yan <i>et al.</i> (1998)
He_I	Yan <i>et al.</i> (1998)
He_{II}	Osterbrock (1989)
Photodissociation:	
H_2	Black & Dalgarno (1977)

Table 2. The main processes responsible for heating and cooling metal-free gas, together with references to the source(s) from which the heating and cooling rates used in our simulations were taken.

3.7 Halting the simulation

Using the method outlined in the preceding sections, we compute the chemical and thermal evolution of the protogalaxy until one of two conditions is met: either the protogalactic gas begins to cool strongly, or we exceed a preset time limit, t_{lim} .

To assess whether gas cooling is ‘strong’ enough requires an objective cooling criterion. A number of different possibilities have been suggested in the literature (Rees & Ostriker 1977; Tegmark *et al.* 1997; Haiman *et al.* 2000). In our simulations, we adopt the criterion used by Haiman *et al.* (2000): we require that the elapsed time exceeds the cooling time, as computed at the edge of the protogalactic core, at a distance $r_0 = 0.034r_t$ from the centre of the protogalaxy. The advantage of this choice is that it avoids giving us a false positive result in cases where t_{cool} drops briefly below t_{dyn} at early times, but remains so for a time $t \ll t_{\text{cool}}$. As an additional sanity check, we also require that the final temperature be smaller than the initial temperature.

If the protogalactic gas does not cool strongly, then the simulation will terminate when it reaches t_{lim} . This pre-set time limit is required on purely practical grounds, to prevent simulations in which the gas does not cool from running for

excessive amounts of time, but also has a physical justification. In our simulations, we treat protogalaxies as isolated objects, uninfluenced by external events. In reality, they are part of a dynamically evolving mass distribution, and the majority will only survive for a limited time before merging with other protogalaxies of a similar or larger size. It is possible to use the Press-Schechter formalism to calculate the distribution of survival times as a function of mass (Lacey & Cole 1993), but for rare objects the mean survival time is typically of the order of the Hubble time and thus for simplicity I set $t_{\text{lim}} = t_{\text{H}}$.

4 RESULTS

In the following sections, we present results from a number of simulations that examine the effects of the X-ray backgrounds produced by the various source models discussed in sections 2.1.3 and 2.1.4. Unless otherwise noted, all of these simulations assume the same parameters for the star formation model: a standard Salpeter IMF, with $M_{\text{min}} = 0.1 M_{\odot}$ and $M_{\text{max}} = 100 M_{\odot}$, a star formation efficiency $\epsilon = 0.1$ and a starburst lifetime $t_{\text{on}} = 10^7$ yr. Additionally, all of the simulations use the same cosmological model, the Λ CDM concordance model of Wang *et al.* (2000), which has parameters $(\Omega_{\Lambda}, \Omega_m, \Omega_b, h, n, \sigma_8) = (0.67, 0.33, 0.041, 0.65, 1.0, 0.9)$.

4.1 Simulations without an X-ray background

Before examining the effect of an X-ray background on protogalactic evolution, we first briefly study the evolution of T_{crit} in its absence. As well as allowing us to determine the sensitivity of our results to variations in the UV source model, this also provides us with a necessary baseline against which to compare our other results.

In figure 2, we plot the evolution of T_{crit} with redshift for the three different star formation models discussed in section 2.1.2. All three models assume a Salpeter IMF, with maximum stellar mass $M_{\text{max}} = 100 M_{\odot}$, as well as our standard star formation efficiency, starburst lifetime and cosmological model, described previously. Our basic model assumes a metal-free stellar population, with a minimum stellar mass of $M_{\text{min}} = 0.1 M_{\odot}$; the corresponding results are given by the dotted line in figure 2. The dashed line illustrates the effect of increasing the minimum mass to $M_{\text{min}} = 1 M_{\odot}$; the solid line assumes the same M_{min} , together with a metallicity $Z = 0.02 Z_{\odot}$.

Figure 2 demonstrates that although the strength of the Lyman-Werner background increases by almost a factor of five as we move from our basic model to the metal-enriched model, this has less effect on T_{crit} than we might expect: the difference in T_{crit} between the three models is never more than 50%, and the qualitative details of its evolution are very similar in all three models. This suggests that the uncertainty introduced by our lack of knowledge of the properties of the primordial stellar population need not be unduly limiting. However, it is also clear that some uncertainty remains, and this will place a lower limit on the magnitude of any effect that we can reliably claim to detect, as small variations in T_{crit} due to the X-ray background will be swamped by the error resulting from the uncertainty in the Lyman-Werner background.

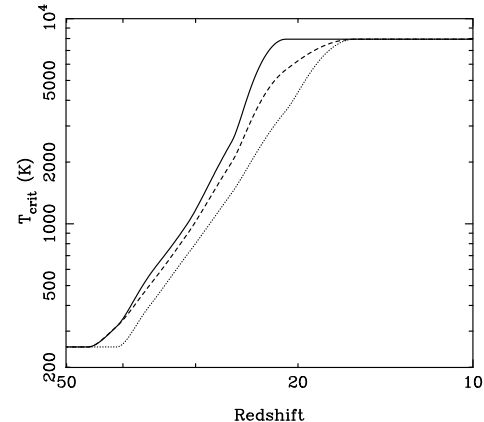


Figure 2. The evolution of the critical temperature as a function of redshift in the absence of an X-ray background. Results are plotted for three different UV source models: two metal-free models, one with a minimum stellar mass $M_{\text{min}} = 0.1 M_{\odot}$ and the other with $M_{\text{min}} = 1 M_{\odot}$ (represented by the dotted and dashed lines respectively) and a $Z = 0.02 Z_{\odot}$ model with $M_{\text{min}} = 1 M_{\odot}$ (solid line). In all three cases, the IMF is of Salpeter form, with a maximum mass $M_{\text{max}} = 100 M_{\odot}$. The remaining parameters of the star formation model (star formation efficiency and starburst lifetime) are the same in all three simulations, as is the cosmological model.

In the work that follows, we take as our baseline the results of our basic, metal-free, low M_{min} model; as figure 2 demonstrates, this minimizes the strength of the Lyman-Werner background, and thus will tend to maximize the effectiveness of the X-ray background.

4.2 Massive X-ray binaries

In figure 3, we plot the evolution of T_{crit} in the presence of the X-ray background generated by the massive X-ray binary model described in section 2.1.3. For the purposes of comparison, we also plot the results of our basic X-ray free model. Initially, the evolution of T_{crit} is the same in both models, implying that the X-ray background has little or no effect on the gas. At a redshift $z \simeq 25$ and critical temperature $T_{\text{crit}} \simeq 2000$ K, however, the models diverge. In the X-ray free model, the critical temperature continues to increase at roughly the same rate until it reaches its maximum value of $T_{\text{crit}} = 8000$ K at a redshift $z \simeq 15$. In the X-ray binary model, by contrast, the rate of increase of T_{crit} is significantly slowed, and it fails to reach its maximum value by the end of the simulation at $z = 10$.⁴

It is clear from figure 3 that the presence of the X-ray background significantly affects the evolution of gas in the larger of the H_2 -cooled protogalaxies. In small protogalaxies, on the other hand, the negative feedback caused by the Lyman-Werner background remains as strong as ever.

⁴ We choose to end our simulations at $z = 10$ because at lower redshift we expect the effects of ionizing radiation from both stellar sources and quasars to become increasingly important and thus our results to become unreliable. Clearly if reionization occurs at $z > 10$, the same is true for some portion of the results plotted here.

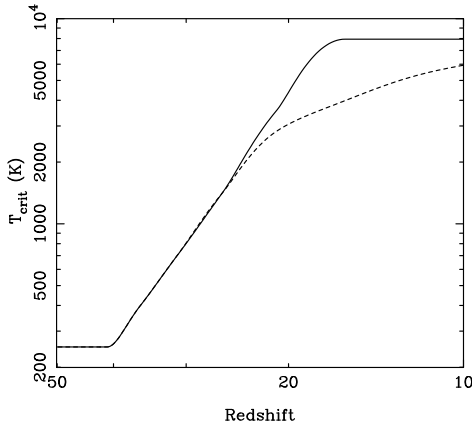


Figure 3. The evolution of T_{crit} as a function of redshift for an X-ray background produced by the massive X-ray binary model of section 2.1.3 (dashed line). For comparison, we also plot the evolution of T_{crit} for our basic X-ray free model (solid line).

A simple way to judge the importance of this effect is to examine the difference it makes to the fraction of gas in the universe that can collapse and cool. As we saw in section 2.1.1, we can use the Press-Schechter formalism to express the cool gas fraction as

$$F(z, M_{\text{crit}}) = \text{erfc} \left[\frac{\delta_c(z)}{\sqrt{2}\sigma(M_{\text{crit}})} \right]. \quad (55)$$

Using the relationship between M_{crit} and T_{crit} derived in that section, it is straightforward to calculate the evolution of $F(z, M_{\text{crit}})$ in both the X-ray binary and X-ray free models.

To better highlight the difference between the two models, we plot in figure 4 the ratio of the cooled gas fraction in the X-ray binary model to that in the X-ray free model. At high redshift, the evolution of T_{crit} is the same in both models, and thus the ratio is one. At $z \sim 25$, the behaviour of the models begins to diverge and the ratio increases, peaking between $z = 20$ and $z = 15$, and subsequently declining as the growth in the cooled mass fraction becomes dominated by the formation of larger protogalaxies that cool via Lyman- α emission.

Figure 4 shows us that by ignoring the effect of the X-ray background we underestimate $F(z, M_{\text{crit}})$ by at most a factor of two. Given the star formation model we have adopted, this corresponds to underestimating the globally-averaged star formation rate by a similar amount. The difference between the two models is potentially greater than this, however, because this extra star formation occurs entirely in low-mass systems, from which ionizing photons (Ricotti & Shull 2000) and supernova ejecta (Ferrara & Tolstoy 2000) can easily escape. Doubling the star formation rate may thus significantly increase the feedback of primordial star formation on the IGM.

Finally, given the uncertainties in the data underlying our simple massive X-ray binary model (see section 2.1.3), it is of interest to investigate the sensitivity of our results to changes in the strength of the X-ray background. Accordingly, we have run additional simulations in which the strength of the X-ray sources was increased or decreased by a factor of ten. The results are plotted in figure 5, together

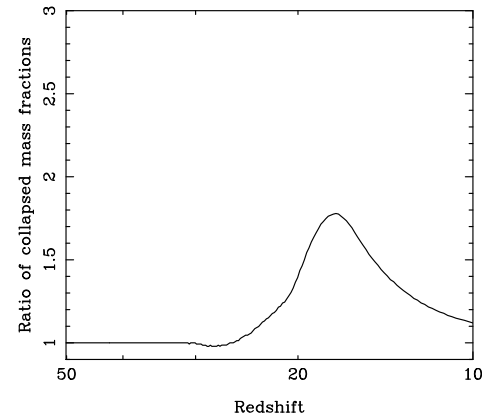


Figure 4. The ratio of the cooled gas fraction in the massive X-ray binary model to that in the X-ray free model. The mass fractions are calculated using the Press-Schechter formalism, as outlined in the text.

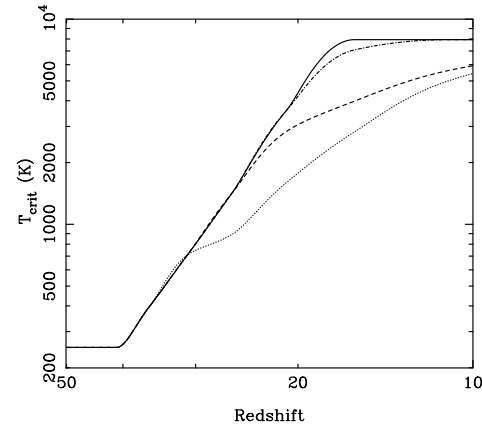


Figure 5. As figure 3, but including variants of the X-ray binary model with 10% (dash-dotted line) and 1000% (dotted line) of the flux of the basic model (dashed line). As before, we also plot the evolution of T_{crit} for the X-ray free model (solid line).

with the results of our basic X-ray binary model and of the X-ray free model.

Unsurprisingly, increasing or decreasing the strength of the X-ray background alters the evolution of T_{crit} . Decreasing it by an order of magnitude increases T_{crit} to the point where its evolution is effectively indistinguishable from that in the X-ray free model. Increasing it by an order of magnitude, on the other hand, systematically lowers T_{crit} , although never by more than a factor of two.

4.3 Supernova remnants

As we discussed in section 2.1.4, it is possible that massive X-ray binaries are much less abundant at high redshift than at the present day. If so, then the X-ray emission of star-forming galaxies will be dominated by supernova remnants (SNR). These will generate X-rays through two main emission mechanisms: thermal bremsstrahlung from hot gas, and inverse Compton scattering of the CMB by relativistic

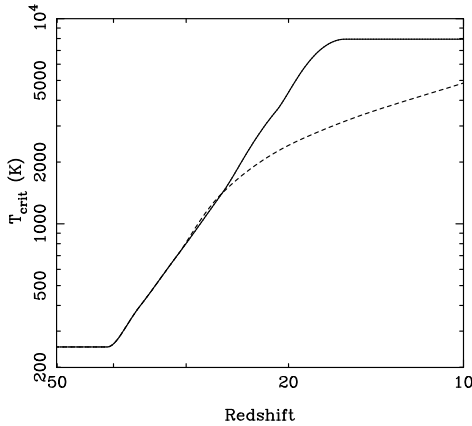


Figure 6. As figure 3, but for an X-ray background produced by inverse Compton emission from supernova remnants. We assume that 10% of the total supernova energy is transferred to the relativistic electrons powering the emission, and again plot the results of the X-ray free model for comparison.

electrons. We consider the effects of these mechanisms separately.

We examined two possible variants of the thermal bremsstrahlung model. In one, we assumed that the characteristics of the emission are broadly the same as those observed locally, with a fraction $f_x = 2 \times 10^{-4}$ of the supernova energy being radiated as X-rays with a characteristic temperature $T_x = 1$ keV (Helfand & Moran 2001). In the other model, we assumed that all high-redshift supernovae explode in extremely dense surroundings, producing X-ray bright, ultra-compact remnants with $f_x = 0.01$ and $T_x = 30$ keV (Terlevich *et al.* 1992). Realistic models should lie somewhere between these two extremes.

However, we found that in neither of these cases does the X-ray background affect the evolution of T_{crit} : at our level of temperature resolution, the results are identical to those obtained for the X-ray free model. The obvious conclusion is that the background produced by bremsstrahlung is simply too weak to be effective.

Our inverse Compton model fares somewhat better. In this model, the strength of the X-ray background is proportional to the mean fraction f_e of the supernova explosion energy that is transferred to relativistic electrons within the remnant. This value is not known accurately and so we considered two possible cases, one with $f_e = 10^{-3}$ and another with $f_e = 0.1$, these being conservative lower and upper bounds on the true value. In the former case, we again saw no significant effect on the evolution of T_{crit} . In the latter case, on the other hand, we saw results very similar to those obtained for the X-ray binary model, as illustrated in figure 6.

In principle, therefore, inverse Compton emission from supernova remnants could be as important an X-ray source as emission from X-ray binaries. Ultimately, however, its importance depends upon the value of f_e , and no firm conclusions are possible until this value is better constrained. In this context, the possible observational tests suggested by Oh (2001) could prove extremely valuable.

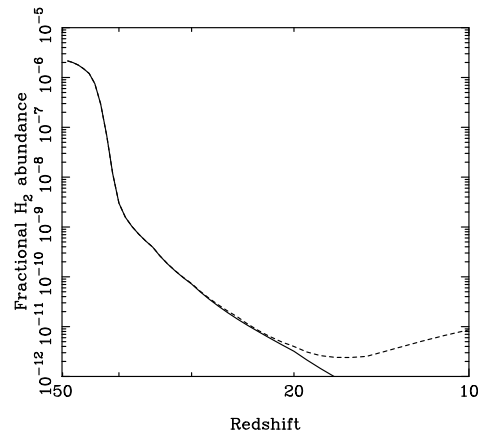


Figure 7. The evolution with redshift of the fractional abundance of H_2 in the intergalactic medium, plotted for the X-ray free model (solid line) and the massive X-ray binary model (dashed line).

4.4 The thermal and chemical evolution of the IGM

As well as determining the evolution of T_{crit} , our simulations also allow us to study the thermal and chemical evolution of the diffuse intergalactic medium, as outlined in section 3.2. As a simple example, we plot in figure 7 the evolution of the fractional H_2 abundance in the IGM for the X-ray free model (solid line) and the X-ray binary model (dashed line).

In both cases, the fractional abundance falls rapidly, reaching $f_{\text{H}_2} = 10^{-9}$ by $z \simeq 35$. Subsequently, its decline slows, in part because the rate of increase in the strength of the ultraviolet background also slows. Below $z = 20$, the behaviour of the two models diverges. In the X-ray free model, f_{H_2} continues to decline until the end of the simulation. In the X-ray binary model, on the other hand, the increasing ionization of the IGM boosts the H_2 formation rate to the point where it overtakes the photodissociation rate and the H_2 abundance, after reaching a minimum at $z \simeq 16$, begins to climb. Nevertheless, it remains extremely small at the end of the simulation, readily justifying our assertion in section 2.2.1 that absorption by intergalactic H_2 does not play a significant role in determining the strength of the Lyman-Werner background.

In figure 8, we plot the evolution of the fractional ionization of the IGM. In the X-ray free model, this remains approximately constant over the lifetime of the simulation, as the recombination timescale is significantly longer than the Hubble time. In the X-ray binary model, on the other hand, photoionization by the growing X-ray background eventually overcomes the very small recombination rate and drives the fractional ionization upwards, increasing it by nearly an order of magnitude by the end of the simulation. Even so, it remains small, demonstrating that the X-ray background does not contribute significantly to cosmological reionization.

The effect on the fractional ionization of helium (the ratio of He^+ to He) is rather more striking. The post-recombination He^+ abundance is extremely small (Stancil *et al.* 1998), and in the X-ray free model remains at this low

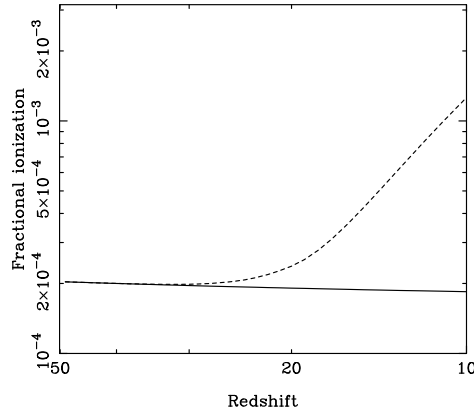


Figure 8. The evolution with redshift of the fractional ionization of the intergalactic medium, plotted for the X-ray free model (solid line) and the massive X-ray binary model (dashed line).

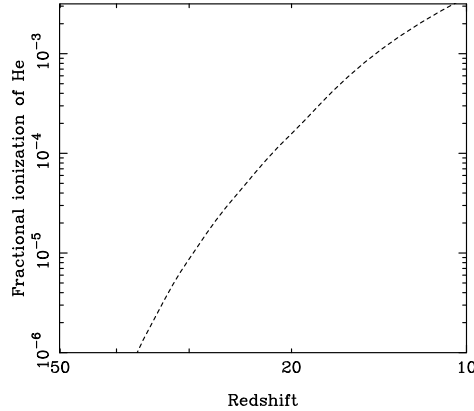


Figure 9. The evolution with redshift of the fractional ionization of helium in the intergalactic medium, plotted for the massive X-ray binary model. In the X-ray free model, the He^+ abundance remains negligible throughout the simulation.

level throughout the simulation. In the X-ray binary model, on the other hand, it increases dramatically over the course of the simulation, reaching $f_{\text{He}^+} = 3.7 \times 10^{-3}$ by $z = 10$. This is illustrated in figure 9.

Finally, in figure 10 we plot the evolution with redshift of the temperature of the IGM. In the X-ray free model, adiabatic cooling dominates the thermal evolution, and the temperature falls off approximately as $(1 + z)^2$. In the X-ray binary model, on the other hand, photo-electric heating begins to heat the IGM strongly at $z = 20$, driving the temperature up to $T = 100$ K by the end of the simulation.

Thus, although the X-ray background does not contribute significantly to the reionization of the IGM, it does produce substantial reheating prior to reionization. Moreover, given the large mean free path of the X-ray photons, this reheating occurs almost uniformly throughout the IGM, rather than being localized to the vicinity of star-forming galaxies.

One consequence of this reheating is that the formation of very small-scale structure will be suppressed, as the increased temperature of the IGM leads to an increased Jeans

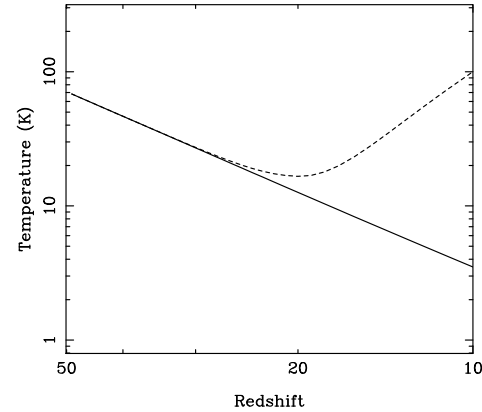


Figure 10. The evolution with redshift of the temperature of the intergalactic medium, plotted for the X-ray free model (solid line) and the massive X-ray binary model (dashed line).

mass. This is unlikely to affect the global star formation rate, however, as star formation within these small structures would in any case be strongly suppressed by the ultraviolet background. Nevertheless, it will reduce the mean clumping factor of the IGM below the level that we would otherwise predict, which may in turn speed up reionization (Haiman *et al.* 2001; Barkana & Loeb 2002).

Reheating also affects the visibility of the IGM in the redshifted 21 cm line of neutral hydrogen. Madau *et al.* (1997) show that scattered Lyman- α emission from high redshift galaxies efficiently couples the spin temperature of the H_1 hyperfine levels to the kinetic temperature of the gas. If the gas temperature is smaller than the CMB temperature, this results in 21 cm line absorption; if it is greater, then it results in emission. Absorption is easier to detect than emission (Scott & Rees 1990), but the heating produced by the X-ray background implies that absorption occurs only at $z \geq 15$, and that concentrating on detecting 21 cm emission may be the more viable strategy.

5 CONCLUSIONS

The results of the previous section allow us to assess the impact of the high redshift X-ray background that is produced by star-forming galaxies. If we assume that the X-ray emission of these galaxies is similar to that observed locally, and that the same correlation between X-ray luminosity and star formation rate applies, then we find that the background produced is strong enough to partially offset the effects of UV photodissociation in large ($T_{\text{vir}} > 1000$ K), H_2 -cooled protogalaxies.

However, local emission is dominated by massive X-ray binaries, which may not form in large numbers at high redshift. Therefore, we have also explored the effect of an X-ray background produced by emission from supernova remnants. If this emission is dominated by inverse Compton scattering and if the fraction of the supernova energy transferred to the relativistic electrons powering this emission is large, then the resulting background has very similar effects to one produced by X-ray binaries. On the other hand, if the frac-

tion of energy transferred is small, then the background has little or no effect.

In addition to inverse Compton emission, we have also examined the effect of thermal bremsstrahlung emission from hot gas in the remnants, and find that even if all supernovae were to form X-ray bright, ultra-compact remnants, the resulting X-ray background would still be too weak to significantly affect protogalactic evolution.

Finally, none of these models produces an X-ray background that is strong enough to balance UV photodissociation in small protogalaxies, with virial temperatures $T_{\text{vir}} < 1000$ K. In these protogalaxies, negative feedback always dominates.

How significant are these results? One simple way to assess this is to study the evolution of the mass fraction of cooled gas, which represents the total amount of matter available to form stars. Comparing its evolution in the X-ray binary model to that in the absence of an X-ray background, we find that it is increased by approximately a factor of two. Given our star formation model, this corresponds to an increase in the global star formation rate by the same amount. However, this is small compared to the order of magnitude increase that would result if we were simply to ignore the effect of the UV background (see figure 7 of Haiman *et al.* 2000).

In reality, the difference between the two models may be greater than this because the additional star formation takes place entirely in low-mass systems, from which ionizing photons and supernova-produced metals can readily escape (Ricotti & Shull 2000; Ferrara & Tolstoy 2000). Doubling the star formation rate may therefore have more than double the impact on the intergalactic medium. However, to properly assess the ultimate importance of this effect requires more detailed modelling, beyond the scope of this paper.

Ultimately, understanding the history of star formation in the small protogalaxies studied in this paper remains important even if they do not contribute to the reionization or enrichment of the IGM to any great degree. This is simply because, in a hierarchical universe, these protogalaxies are the building blocks from which larger galaxies form and therefore set the initial conditions for later stages of galaxy formation. In particular, very little metal enrichment of the primordial gas is required in order to allow the CNO cycle to operate and population II (rather than population III) stars to form, and yet this can have a profound affect on the predicted spectral energy distribution of an early stellar population.

Although the main purpose of our study was to examine the effects of the X-ray background on the thermal and chemical evolution of gas within protogalaxies, our approach also allows us to examine the effects of the background on the diffuse IGM. Our main results are three-fold:

(i) We confirm the rapid destruction of H₂ in the intergalactic medium noted by Haiman *et al.* (2000), but also show that when an X-ray background is present the H₂ abundance does not continue to decline indefinitely, but eventually stabilizes and may even begin to increase. However, it never becomes large enough to significantly affect the Lyman-Werner background.

(ii) We show that although photoionization by the X-ray background significantly increases the fractional ionization

of the IGM (and in particular the fractional ionization of helium), the bulk of the gas remains mostly neutral, demonstrating that the contribution of the X-ray background to cosmological reionization is small.

(iii) We find that the X-ray background will also heat the intergalactic gas, raising its temperature to $T \simeq 100$ K by $z = 10$ (compared to $T = 3.5$ K in the X-ray free model). This will suppress the formation of structure on the smallest scales by increasing the Jeans mass. It is unlikely to affect the global star formation rate, since $T_{\text{crit}} \gg 100$ K, but may speed up the process of reionization by reducing the mean clumping factor of the IGM.

In closing, we note that a number of uncertainties still remain in our treatment of this problem. Some of these – the high redshift star formation rate or the appropriate population III initial mass function, for instance – we simply do not know at the present time. Fortunately, changes to our assumed values can be readily incorporated in the framework laid out in this paper. Other uncertainties arise from our method of simulation; in particular, from our assumption of a static density profile for the protogalactic gas. We hope to address these issues in future work.

ACKNOWLEDGMENTS

SCOG would like to acknowledge useful discussions about various aspects of this work with Tom Abel, Omar Almaini, Rennan Barkana, Marie Machacek and Si Peng Oh. SCOG also acknowledges financial support by a PPARC studentship.

REFERENCES

- Abel, T., Anninos, P., Zhang, Y., Norman, M. L., 1997, *New Astron.*, 2, 181.
- Abel, T., Bryan, G. L., Norman, M. L., 2000, *ApJ*, 540, 39.
- Aggarwal, K. M., Callaway, J., Kingston, A. E., Unnikrishnan, K., 1992, *ApJS*, 80, 473.
- Aldrovandi, S. M. V., Pequignot, D., 1973, *A&A*, 25, 137.
- Barkana, R., Loeb, A., 2002, *astro-ph/0204139*.
- Bates, D. R., Öpik, U., 1968, *J. Phys. B*, 1, 543.
- Black, J. H., Dalgarno, A., 1977, *ApJS*, 34, 405.
- Brandt, W. N., Hornschemeier, A. E., Schneider, D. P., Alexander, D. M., Bauer, F. E., Garmire, G. P., Vignali, C., 2001, *ApJ*, 558, L5.
- Bray, I., Burgess, A., Fursa, D. V., Tully, J. A., 2000, *A&AS*, 146, 481.
- Bromm, V., Coppi, P. S., Larson, R. B., 1999, *ApJ*, 527, L5.
- Bromm, V., Coppi, P. S., Larson, R. B., 2002, *ApJ*, 564, 23.
- Cassisi, S., Castellani, V., 1993, *ApJS*, 88, 509.
- Cen, R., 1992, *ApJS*, 78, 341.
- Chevalier, R. A., 1999, *ApJ*, 511, 798.
- Ciardi, B., Ferrara, A., Governato, F., Jenkins, A., 2000, *MNRAS*, 314, 611.
- Ciardi, B., Ferrara, A., Abel, T., 2000, *ApJ*, 533, 594.
- Cojazzi, P., Bressan, A., Lucchin, F., Pantano, O., Chavez, M., 2000, *MNRAS*, 315, L51.

Couchman, H. M. P., Rees, M. J., 1986, MNRAS, 221, 53.

Dalgarno, A., Yan, M., Liu, W., 1999, ApJS, 125, 237.

David, L. P., Jones, C., Forman, W., 1992, ApJ, 388, 82.

de Jong, T., 1972, A&A, 20, 263.

Draine, B. T., Bertoldi, F., 1996, ApJ, 468, 269.

Dunn, G. H., 1968, Phys. Rev., 172, 1.

Ezer, D., Cameron, A. G. W., 1971, ApSS, 14, 399.

Ferland, G. J., Peterson, B. M., Horne, K., Welsh, W. F., Nahar, S. N., 1992, ApJ, 387, 95.

Ferrara, A., Tolstoy, E., 2000, MNRAS, 313, 291.

Fuller, T. M., Couchman, H. M. P., 2000, ApJ, 544, 6.

Galli, D., Palla, F., 1998, A&A, 335, 403.

Gerlich, D., 1990, J. Chem. Phys., 92, 2377.

Ghosh, P., White, N. E., 2001, ApJ, 559, L97.

Glover, S. C. O., 2001. Ph.D. thesis, Edinburgh University.

Glover, S. C. O., Brand, P. W. J. L., 2001, MNRAS, 321, 385.

Haiman, Z., Loeb, A., 1997, ApJ, 483, 21.

Haiman, Z., Thoul, A. A., Loeb, A., 1996, ApJ, 464, 523.

Haiman, Z., Rees, M. J., Loeb, A., 1996, ApJ, 467, 522.

Haiman, Z., Rees, M. J., Loeb, A., 1997, ApJ, 476, 458.

Haiman, Z., Madau, P., Loeb, A., 1999, ApJ, 514, 535.

Haiman, Z., Abel, T., Rees, M. J., 2000, ApJ, 534, 11.

Haiman, Z., Abel, T., Madau, P., 2001, ApJ, 551, 599.

Halford, D. J., Moran, E. C., 2001, ApJ, 554, 27.

Holliday, M. G., Muckerman, J. T., Friedman, L., 1971, J. Chem. Phys., 54, 1058.

Hummer, D. G., Storey, P. J., 1998, MNRAS, 297, 1073.

Huq, M. S., Doverspike, L. D., Champion, R. L., Esaulov, V. A., 1982, J. Phys. B., 15, 951.

Janev, R. K., Langer, W. D., Evans, K., Post, D. E., 1987. *Elementary Processes in Hydrogen-Helium Plasmas*. Springer.

Karpas, Z., Anicich, V., Huntress, W. T., 1979, J. Chem. Phys., 70, 2877.

Kepner, J. V., Babul, A., Spergel, D. N., 1997, ApJ, 487, 61.

Kimura, M., Lane, N. F., Dalgarno, A., Dixson, R. G., 1993, ApJ, 405, 801.

Kudritzki, R. P., in *The First Stars*, eds. A. Weiss, T. Abel, and V. Hill, Springer, 2000.

Lacey, C., Cole, S., 1993, MNRAS, 262, 627.

Larson, R. B., 1998, MNRAS, 301, 569.

Launay, J. M., Le Dourneuf, M., Zeippen, C. J., 1991, A&A, 252, 842.

Le Bourlot, J., Pineau des Forets, G., Flower, D. R., 1999, MNRAS, 305, 802.

Leitherer, C., Heckman, T. M., 1995, ApJS, 96, 9.

Lenzuni, P., Chernoff, D. F., Salpeter, E. E., 1991, ApJS, 76, 759.

Loeb, A., Barkana, R., 2001, ARA&A, 39, 19.

Machacek, M. E., Bryan, G. L., Abel, T., 2001, ApJ, 548, 509.

Madau, P., Meiksin, A., Rees, M. J., 1997, ApJ, 475, 429.

Madau, P., Haardt, F., Rees, M. J., 1999, ApJ, 514, 648.

Martin, P. G., Schwarz, D. H., Mandy, M. E., 1996, ApJ, 461, 265.

Meurs, E. J., van den Heuvel, E. P. J., 1989, A&A, 226, 88.

Moseley, J., Aberth, W., Peterson, J. A., 1970, Phys. Rev. Lett., 24, 435.

Natarajan, P., Almaini, O., 2000, MNRAS, 318, L21.

Oh, S. P., 2001, ApJ, 553, 499.

Omukai, K., Nishi, R., 1999, ApJ, 518, 64.

O'Neil, S. V., Reinhardt, W. P., 1978, J. Chem. Phys., 69, 2126.

Osterbrock, D. E., 1989. *Astrophysics of Gaseous Nebulae and Active Galactic Nuclei*. University Science Books.

Peebles, P. J. E., 1993. *Principles of Physical Cosmology*. Princeton University Press.

Pei, Y. C., 1995, ApJ, 438, 623.

Poulaert, G., Brouillard, F., Claeys, W., McGowan, J. W., Wassenhove, G. V., 1978, J. Phys. B, 11, L671.

Press, W. H., Schechter, P., 1974, ApJ, 187, 425.

Press, W. H., Flannery, B. P., Teukolsky, S. A., Vetterling, W. T., 1986. *Numerical Recipes: The Art of Scientific Computing*. CUP.

Ramaker, D. E., Peek, J. M., 1976, Phys. Rev. A, 13, 58.

Rees, M. J., Ostriker, J. P., 1977, MNRAS, 179, 541.

Rephaeli, Y., Gruber, D., Persic, M., 1995, A&A, 300, 91.

Ricotti, M., Shull, J. M., 2000, ApJ, 542, 548.

Ricotti, M., Gnedin, N. Y., Shull, J. M., 2001, astro-ph/0110431.

Ricotti, M., Gnedin, N. Y., Shull, J. M., 2001, astro-ph/0110432.

Samson, J. A. R., Haddad, G. N., 1994, J. Opt. Soc. Am. B, 11, 277.

Schaerer, D., 2002, A&A, 382, 28.

Schneider, I. F., Dulieu, O., Giusti-Suzor, A., Roueff, E., 1994, ApJ, 424, 983.

Scott, D., Rees, M. J., 1990, MNRAS, 247, 510.

Shapiro, P. R., Kang, H., 1987, ApJ, 318, 32.

Shapiro, P. R., Iliev, I. T., Raga, A. C., 1999, MNRAS, 307, 203.

Shapley, A. E., Steidel, C. C., Adelberger, K. L., Dickinson, M., Giavalisco, M., Pettini, M., 2001, ApJ, 562, 95.

Spitzer, L., 1978. *Physical Processes in the Interstellar Medium*. Wiley.

Stancil, P. C., Lepp, S., Dalgarno, A., 1998, ApJ, 509, 1.

Stecher, T. P., Williams, D. A., 1967, ApJ, 149, L29.

Stibbe, D. T., Tennyson, J., 1999, ApJ, 513, L147.

Tegmark, M., Silk, J., Rees, M., Blanchard, A., Abel, T., Palla, F., 1997, ApJ, 474, 1.

Terlevich, R., Tenorio-Tagle, G., Franco, J., Melnick, J., 1992, MNRAS, 255, 713.

Tumlinson, J., Shull, J. M., 2000, ApJ, 528, L65.

Wang, L., Caldwell, R. R., Ostriker, J. P., Steinhardt, P. J., 2000, ApJ, 530, 17.

Wilms, J., Allen, A., McCray, R., 2000, ApJ, 542, 914.

Wishart, A. W., 1979, MNRAS, 187, 59P.

Yan, M., Sadeghpour, H. R., Dalgarno, A., 1998, ApJ, 496, 1044.

Zygelman, B., Dalgarno, A., Kimura, M., Lane, N. F., 1989, Phys. Rev. A, 40, 2340.